The Astronomical Journal, 139:1117–1127, 2010 March doi:10.1088/0004-6256/139/3/1117

PLUTO AND CHARON WITH THE *HUBBLE SPACE TELESCOPE*. I. MONITORING GLOBAL CHANGE AND IMPROVED SURFACE PROPERTIES FROM LIGHT CURVES

Marc W. Buie[1], William M. Grundy[2], Eliot F. Young[1], Leslie A. Young[1], and S. Alan Stern[1]
[1] SwRI, 1050 Walnut Street, Suite 300, Boulder, CO 80302, USA; buie@boulder.swri.edu, efy@boulder.swri.edu, layoung@boulder.swri.edu, alan@boulder.swri.edu
[2] Lowell Observatory, 1400 W. Mars Hill Road, Flagstaff, AZ 86001, USA; grundy@lowell.edu
Received 2009 May 29; accepted 2009 November 18; published 2010 February 4

ABSTRACT

We present new light-curve measurements of Pluto and Charon taken with the Advanced Camera for Surveys High-resolution Camera on the *Hubble Space Telescope*. The observations were collected from 2002 June to 2003 June at 12 distinct sub-Earth longitudes over a range of solar phase angle 0.°36–1.°74—a larger range than previously measured. The new measurements of Pluto show that the light-curve amplitude has decreased since the mutual event season in the late 1980s. We also show that the average brightness has increased in the F555W (Johnson *V* equivalent) passband while the brightness has decreased in the F435W (Johnson *B* equivalent) passband. These data thus indicate a substantial reddening of the reflected light from Pluto. We find a weighted mean $(B-V) = 0.9540 \pm 0.0010$ that is considerably higher than the long-standing value of $(B-V) = 0.868 \pm 0.003$ most recently measured in 1992–1993. This change in color cannot be explained by the evolving viewing geometry and provides the strongest evidence to date for temporal changes on the surface of Pluto that are expected to be linked to volatile transport processes. We also report on the discovery of a new rotational modulation of Pluto's hemispherical color that ranges from 0.92 to 0.98 with the least red color at the longitude of maximum light and most red at minimum light. The phase coefficient of Pluto is nearly the same as measured in 1992–1993 with a value of $\beta_B = 0.0392 \pm 0.0064$ and $\beta_V = 0.0355 \pm 0.0045$ mag deg^{-1} for the F435W and F555W data, respectively. The Pluto phase curve is still very close to linear but a small but significant nonlinearity is seen in the data. In contrast, the light curve of Charon is essentially the same as in 1992/1993, albeit with much less noise. We confirm that Charon's Pluto-facing hemisphere is 8% brighter than the hemisphere facing away from Pluto. The color of Charon is independent of longitude and has a mean weighted value of $(B-V) = 0.7315 \pm 0.0013$. The phase curve for Charon is now shown to be strongly nonlinear and wavelength dependent. We present results for both Pluto and Charon that better constrain the single-particle scattering parameters from the Hapke scattering theory.

Key words: planets and satellites: individual (Charon, Pluto) – planets and satellites: surfaces

Online-only material: color figures, machine-readable and VO table

1. INTRODUCTION

So far our understanding of Pluto and its largest moon, Charon, is a consequence of remote sensing largely from light reflected or emitted from its surface. Arguably the easiest measurement to make of this distant world is photometry. The photometric record now extends back to the time of Pluto's discovery in 1930 (see reviews by Marcialis 1997; Binzel & Hubbard 1997; Buie et al. 1997b). Even though this record lacks spatial resolution (not even to separate Pluto from Charon in most cases), it still provides a critical top-level constraint on the global surface properties. In principle, this record also holds the key to understanding seasonal variations of the atmosphere over the course of its year. The eccentricity of Pluto's orbit, coupled with its large obliquity, causes substantial variations in the solar insolation that should lead to profound surface and atmospheric variations (Hansen & Paige 1996). Unfortunately, as the illuminating geometry changes so does the viewing geometry. These geometric considerations cause rather large modulations in the photometry that have nothing to do with global change. Therefore, to understand seasonal variability we must be able to disentangle the geometric from the temporal photometric variation.

Normally, all interpretations of light curve (i.e., spatially unresolved) observations are complicated by geometry but a new measurement of old data has finally broken the indeterminacy. Schaefer et al. (2008) were able to extract photometry from photographic plates taken shortly after Pluto's discovery in 1930. They showed that the mean albedo for the same range in latitude was 5% brighter than was inferred from the 1954 light curve of Walker & Hardie (1955). Unlike any other pair of observational epochs, the viewing geometry in 1930 and 1954 was nearly identical. The only external change over the intervening two decades was a decrease in the heliocentric distance by 5 AU. The photometry thus reveals a period of global darkening of Pluto's surface. At the time, the viewing geometry was such that Pluto was viewed nearly pole on; thus this decrease would argue strongly for a darkening of this sunlit pole. Stern et al. (1988) warned that the surface would exhibit global atmospherically induced change, and it appears that prediction has now been confirmed by observational data. As we continue to expand the observational record on Pluto, this time variability will need to be an important component of any model description.

In the early 21st century, Pluto had recently passed perihelion and the solar illumination was moving to the opposite pole as was seen in 1933. A common misconception is that change on Pluto at this time should have been driven by its increasing heliocentric distance. However, perihelion is defined as the time where the first derivative of the heliocentric distance is *zero,* and thus is an epoch of nearly constant distance, rather than strongly varying distance. Instead, the mean longitude of Pluto around

Table 1
Summary of ACS Observations

Visit No.	Elon^T (deg)	Visit Start (UT)	Duration (B,V H:M)	r (AU)	Δ (AU)	g (deg)	OTAT (deg)
1	000	2002 Jun 11 07:43	0:26,1:14	30.518	29.521	0.36	−24.2
7	180	2002 Jun 14 12:39	0:26,1:14	30.519	29.527	0.41	−31.6
3	060	2002 Jun 18 17:40	0:26,1:17	30.521	29.539	0.50	−43.0
5	120	2002 Jul 02 13:28	0:26,1:11	30.526	29.615	0.86	−66.4
9	240	2002 Jul 17 10:54	0:26,1:12	30.532	29.751	1.24	−71.0
11	300	2002 Oct 03 03:59	0:26,1:11	30.561	30.956	1.71	−88.2
6	150	2003 Feb 18 00:49	0:21,0:20	30.613	30.944	1.73	96.4
2	030	2003 Apr 20 17:46	0:21,1:08	30.637	29.983	1.44	86.2
8	210	2003 May 13 02:11	0:21,1:07	30.646	29.757	0.91	76.6
12	330	2003 May 28 02:11	0:21,0:20	30.651	29.675	0.51	67.6
4	090	2003 May 30 02:48	1:11,0:31	30.652	29.668	0.46	56.1
10	270	2003 Jun 08 17:13	1:11,0:20	30.656	29.655	0.32	8.5

(This table is available in its entirety in machine-readable and Virtual Observatory (VO) forms in the online journal. A portion is shown here for guidance regarding its form and content.)

the Sun is at its peak rate of change leading to a correspondingly rapid change in viewing and illumination geometry. An excellent summary of these geometric considerations can be found in Hansen & Paige (1996). The important context for these observations is that they take place when Pluto is changing from an equatorial to polar aspect. The visible pole is becoming an ever-increasing systematic source of volatiles as the winter pole traps sublimated material and removes it from view. At this time, we can expect a certain degree of evolution in the visible surface but it is difficult to predict the exact outcome of this variation (Hansen & Paige 1996; Trafton et al. 1998). The albedo could be changing as bright ice is removed from view, leaving behind darker immobile material. Such a variation might also lead one to expect changes in spectral signatures and perhaps the color of the surface. Additionally, the volatile migration pattern during this change could lead to interesting evolution in the surface properties such as grain size and macroscopic texture and thus scattering behavior (Grundy & Stansberry 2000). This change could in turn produce either an increase or a decrease in albedo and thus change the amount of energy input into the system from solar illumination.

Interpretations of other data sets will be improved by a firm understanding of the basic properties of Pluto's light curve. Spectroscopic studies (Grundy & Buie 2001) can directly monitor some volatiles: is the isolated CO-rich spot near light curve maximum surviving over time; is CH_4 migrating or getting covered over; and is N_2 being depleted in visible terrains? The best results from this type of work will come from understanding the absolute albedo trends as well as knowing how to remove the Charon signal from the total flux. Models that would purport to describe the current epoch of volatile migration require knowledge of the energy being input into the system and thus the global albedo with rotation. All of these elements of study come together when trying to understand the wealth of information from stellar occultation observations of Pluto's atmosphere (Young et al. 2008), not the least of which is that the surface is clearly a critical lower boundary to the atmosphere.

This paper is the first in a two-part series and presents detailed light-curve observations for Pluto and Charon as separate objects. The second paper (Paper II) delves into the disk-resolved results of the data. These works were based on observations taken with the then new Advanced Camera for Surveys (ACS) in the High-resolution Camera (HRC) operating on the *Hubble Space Telescope* (*HST*) taken in 2002–2003. Here, we present a description of the observations and move on to discuss disk-integrated light measurements. We also provide a new epoch of separate light curves, colors, and photometric variations with respect to solar phase angle that are then used also to constrain surface particle scattering properties.

2. OBSERVATIONS

Our observing program, GO9391, on *HST* was allocated 12 orbits in 2002–2003 with ACS/HRC to image the Pluto–Charon system. As it happens, these observations also contained information on the since-discovered small satellites, Nix and Hydra. Those results can be found in Buie et al. (2006) and Tholen et al. (2008). The primary goal of these observations was to extract a two-color map of Pluto. That portion of the work can be found in Paper II. The goals of the imaging program dominated the structure of the observations but also improved the return from the photometry. The observations were carried out while *HST* was operating in full three-gyro stabilized mode.[3]

2.1. Visit Timing

All data were taken from 2002 June to 2003 June, and the visits are summarized in Table 1. In this table, we list each visit in order of time of observation along with the targeted longitude (Elon^T), UT start time of the visit, visit duration (B then V), heliocentric distance r, geocentric distance Δ, solar phase angle g, and finally the spacecraft orientation OTAT (derived from the ORIENTAT header keyword that gives the roll angle of *HST*). Each visit was designed to occur at a specific sub-Earth longitude (Elon^T) on Pluto.[4] We targeted a 30° longitude spacing to provide uniform coverage in our 12 visits. The visits were scattered throughout cycle 11 so that the spacecraft roll angle would vary as much as possible over the visits to make the map inversions more robust. This constraint also naturally led to the

[3] Three-gyro tracking is often viewed as being critical to the guiding and tracking performance of *HST*. In recent years, two-gyro tracking has been shown to be nearly identical in the delivered image quality and is often considered to be an operating mode with a low science impact. Two-gyro mode, however, imposes stringent limits on observing geometry, and this program would not have been possible without three-gyro operations.

[4] For this work, we use the same coordinate system for Pluto and Charon as in Buie et al. (1997) and Stern et al. (1997) that is a right-handed coordinate system (hence east longitude), and the north pole is in the direction of the rotational angular momentum. The 0° longitude passes through the sub-Pluto point on Charon and the sub-Charon point on Pluto at periapse.

maximum possible range of solar phase angles. The timing of the observations was further crafted so that the first six visits would occur in the first half of the year prior to solar conjunction and these six could be used for a complete map with 60° longitude spacing. The last six orbits then comprised another complete sampling of the globe with a 30° shift relative to the first half. Additional care was taken to make sure some observations were scheduled during the roughly one-week period each year where the solar phase angle was less than 0.°4. This visit timing pattern is particularly valuable in that the phase dependence can be cleanly decoupled from the light curve, and all phase angles are replicated in the two halves of the data set. The success of these observations was in no small way due to the exceptional effort and care in scheduling provided by Andy Lubenow at STScI.

2.2. Visit Pattern

Each visit incorporated an identical sequence of observations and was designed to fit in a single *HST* visibility window (though visits 6 and 12 were the only ones where the sequence actually ended up executing in a single visibility window). The key to obtaining the full diffraction-limited resolution results was a thorough dithering strategy which consisted of a sixteen-exposure pattern. This pattern optimally fills a unit pixel cell with 16 unique fractional *X* and *Y* positions combined with a larger 80 pixels pattern to guard against localized problems with the detector. Each visit was filled with one pattern of 12 s exposures with the F435W filter followed by an identical pattern of 6 s exposures with the F555W filter.[5] Interleaving the filters would have been better, but the extra overhead was prohibitively high. As shown in Table 1, the F435W observations almost always fell within a single visibility window and when they did the 16 images span 26 min or less. Two visits, 4 and 10, executed so that the F435W observations were split across two visibility windows thus spreading them out in time by 71 min. In contrast, the F555W observations were usually split across two visibility windows. For the purposes of mapping the surface, these issues are unimportant but proper analysis of the light-curve data requires careful correction for these timing issues. Exposure times were chosen to provide a peak signal of 50% of saturation on Pluto assuming it to be centered on a pixel, at maximum light, and at a phase angle of 0.°6.

Full-frame readout for this observing cadence was not possible due to data rate and onboard storage limitations. Instead, we read out the central 512 rows of each image for a net image size of 1024 × 512. This field of view is still substantially larger than the Pluto system plus the dithering pattern. At the time our observations were obtained this was not a fully supported operating mode, so we took bias frames with the same sub-array at each visit. The on-the-fly data processing pipeline at STScI uses a bias frame derived from a full-frame readout of the CCD. We tested our partial-frame readout bias frames against the pipeline calibration frames and found no differences. As a result, all of our data are simply the output of the calibration pipeline from STScI and were extracted for final analysis at least three months after collection so that the best available calibration products would be used. Images that are processed within a few days of observation often use predictive calibration products that are not quite as good as the final calibration files. Finally, the photometric measurements are all calibrated based one the most recent value for PHOTFLAM as of the time of publication (5.36856×10^{-19} for F435W and 3.02007×10^{-19} for F555W both in erg cm^{-2} Å electron^{-1}).

[5] Throughout this work, we use *B* interchangeably with F435W and *V* with F555W. The instrumental filters used are the closest matches to the standard Johnson filters, and we convert to standard passband fluxes as appropriate.

3. PHOTOMETRY

This data set was designed for mapping the surface of Pluto and the resulting map can be used to infer a light curve. However, direct integration of the detected signal also provides information on the disk-integrated photometric properties in a much more straightforward manner. The flux-calibrated map can be used to cross-check the photometric results but we prefer the aperture photometry for investigations of the light curve. This section describes how we extracted aperture-photometry-based light curve measurements.

3.1. Aperture Extraction

We used a 2.5 pixels (∼65 mas) radius aperture centered on the center of light of each object. The choice of aperture was a compromise between including the object being measured while excluding the signal from the other object and is also slightly larger than the disk of Pluto. The small sky signal in each image was removed before integration by computing a robust mean for the entire image and then subtracting. Next, the image was corrected by multiplying by the pixel area map (described in more detail later). Also, before measuring each object (Pluto or Charon), the other object was subtracted from the image so that the photometry is not corrupted by their overlapping point-spread functions (PSFs). To do this for measuring Pluto, the Charon model image was computed and then subtracted from the sky-subtracted image. Similarly, a model Pluto was computed and then subtracted before measuring Charon. The flux "correction" to Pluto by subtracting Charon was weakly correlated with sub-Earth longitude and never higher than 0.1% with an average correction of 0.04%. The correction to the Charon photometry was understandably higher and strongly correlated with its projected distance from Pluto with a correction of 1.9% near minimum separation and 0.2% near maximum separation. The model used was the one described in detail in Paper II but note that given the size of the correction the model only needs to be close to the truth to make the error in the correction negligible.

Our small aperture integration is described in Buie & Bus (1992). This technique worked well for small apertures but makes a necessary assumption that the incident flux distribution on a pixel is uniform. A useful check on the model fitting process was to measure the residual flux on either Pluto or Charon after both have been subtracted from the image. This check uses the exact same location as for the photometric extraction. For Pluto, the mean of the residual flux is 0.5% of the total flux of Pluto with a standard deviation of 1.5%. For Charon, the mean residual flux is 2% with a standard deviation of 2%. The standard deviation is an indicator of the photometric accuracy of the model on an individual frame.

3.2. Aperture Corrections

ACS is an off-axis instrument on *HST*. As a result of being off-axis combined with the instrumental optical correction of the original spherical aberration of the telescope, the image recorded by the detector suffers from severe, but well-calibrated, geometric distortions relative to the plane of the sky. These distortions must be accounted for in order to retrieve most results from the data. The PSF of the telescope is also important and

Table 2
Visit-averaged *B* Photometry of Pluto

JD Mid-time	*g* (deg)	Lat (deg)	Elon (deg)	*B* (mag)	Rotation Mag	Phase Mag
2452436.830645	0.361	29.38	0.55	16.3039(17)	16.2886	16.2909
2452787.598492	0.513	31.63	28.61	16.3445(03)	16.3223	16.3057
2452550.675166	1.712	28.33	64.21	16.4546(06)	16.3828	16.3538
2452799.240041	0.316	31.35	92.59	16.4534(14)	16.4402	16.3067
2452472.962867	1.238	28.55	124.38	16.4571(05)	16.4038	16.3349
2452772.598087	0.912	31.96	153.91	16.3593(09)	16.3196	16.3288
2452440.035934	0.410	29.30	179.93	16.2238(04)	16.2063	16.2994
2452688.541026	1.734	32.17	211.52	16.2058(10)	16.1331	16.3608
2452458.069952	0.858	28.86	243.66	16.2068(04)	16.1694	16.3200
2452789.643255	0.464	31.58	273.38	16.2577(14)	16.2377	16.3092
2452444.244973	0.499	29.19	302.74	16.2669(08)	16.2454	16.3034
2452750.247484	1.443	32.33	333.47	16.3285(06)	16.2671	16.3453

Table 3
Visit-averaged *V* Photometry of Pluto

JD Mid-time	*g* (deg)	Lat (deg)	Elon (deg)	*V* (mag)	Rotation Mag	Phase Mag
2452436.862716	0.361	29.38	358.75	15.3460(30)	15.3322	15.3453
2452787.613817	0.513	31.63	27.75	15.3909(04)	15.3707	15.3508
2452550.702273	1.712	28.33	62.68	15.4945(09)	15.4284	15.3990
2452799.274918	0.316	31.35	90.63	15.4712(09)	15.4592	15.3389
2452472.996286	1.238	28.55	122.50	15.4924(09)	15.4435	15.3854
2452772.634032	0.911	31.96	151.89	15.3719(13)	15.3356	15.3539
2452440.068009	0.411	29.30	178.12	15.2808(04)	15.2648	15.3477
2452688.556350	1.734	32.17	210.66	15.2690(11)	15.2021	15.3920
2452458.097114	0.859	28.86	242.13	15.2661(07)	15.2318	15.3665
2452789.676579	0.463	31.58	271.51	15.2976(09)	15.2794	15.3475
2452444.277588	0.500	29.19	300.90	15.3213(09)	15.3016	15.3508
2452750.264898	1.442	32.33	332.49	15.3632(04)	15.3068	15.3872

must be considered but most of the computational work was a consequence of the distortions. For this work, we made extensive use of TinyTim version 6.2 (Krist 2004) to generate the PSFs and to correct for the optical distortions.

We learned valuable lessons concerning the behavior of the ACS camera. First, the PSF is clearly dependent on the filter, as one would expect, but it also depends on the color of the object being imaged. Therefore, we chose computed reference PSFs for this work with a TinyTim color of 12 for Charon ($(B-V)=0.66$) and 14 for Pluto ($(B-V)=0.92$). Additionally, we found that the PSF itself is constant over the field of view of the camera. However, when combined with the optical distortions, the effective PSF in the sampled images varies significantly with position. The calculations are supported by a pre-computed library of numerical PSFs computed on a 50 pixels grid. When applying a PSF correction to a location in the image, the nearest PSF was fetched from the library to help speed up the computations.

Another important step is the use of a "pixel-area map" (PAM). The STScI pipeline processing returns an image that preserves surface brightness. To properly extract fluxes from an image containing isolated sources, whether by PSF fitting or aperture summation, one must first subtract the sky and then multiply by the PAM to restore the actual counts from the sources. The easiest way to think of this is that the pipeline images are a measure of counts per unit area where the unit area is the adopted (constant) size of a pixel. This correction is doubly important. First, the adopted pixel area is not the same or even close to the true average pixel area. Thus, the PAM makes a substantial ($\sim$12%) systematic correction to the inferred point-source fluxes. Second, the pixel size is not constant across the field of view, and the PAM corrects a $\pm$2% variation across the image.

Lastly, the result from the aperture integration is an instrumental flux (or magnitude) for Pluto and Charon in each filter. The small photometry aperture used requires correction to an infinite aperture flux. The correction is substantial and depends on an effect known as "breathing." During each orbit, the temperature of the telescope structure varies and causes the telescope to be slightly out of focus in proportion to the changing temperature. If not corrected, this will cause as much as a 4% error in the photometry (relative to nominal focus). To correct for breathing, we computed a TinyTim PSF at the fitted focus position (see Paper II for details) for each image. From this numerical PSF, we compute the ratio of the 2.5 pixels aperture flux to the total flux. The position of the aperture is forced to be at the location of the peak as determined from finding the interpolated maximum of the PSF. This ratio is the aperture correction that converts our small-aperture photometry to effectively infinite aperture photometry.

3.3. Transformation

The infinite aperture fluxes are then converted to standard Johnson passbands using the transformation relationships and coefficients from Siriani et al. (2005). This calculation is slightly more complicated because one must solve for the standard color of the object after transformation. In practice, it works to guess a color, compute the final photometry and thus a new color, use the new color to recompute the transformation, and iterate until the results (photometry and colors) converge. At this step, the final converged colors were $(B-V)=0.9584\pm0.0023$ for Pluto and $(B-V)=0.7327\pm0.0019$ for Charon, and were used for all transformation calculations. The difference in the transformation between these values and the final colors derived later is negligible. The last measured separate colors are $(B-V)=0.8675\pm0.0014$ for Pluto and $(B-V)=0.710\pm0.011$ (Buie et al. 1997). The difference in the final magnitudes using either the old or new colors is less than 1%.

Finally, the observed apparent magnitudes were all corrected to mean opposition distance ($r=39.5$ AU and $\Delta=38.5$ AU) in keeping with past publications of Pluto photometry. Normally, one would also correct for solar phase angle at this point. However, we wish to investigate the phase behavior, so this correction is not included in the tabulated photometry.

4. LIGHT-CURVE ANALYSIS

The visit-averaged photometry for Pluto is tabulated in Tables 2 and 3 while the Charon photometry is tabulated in Tables 4 and 5. Each table contains the mid-time of the observation, solar phase angle, sub-Earth latitude, and sub-Earth east longitude computed from a mean of the individual measurements. The tabulated magnitudes are the mean of the visit corrected to mean opposition distance with no solar phase angle correction. The uncertainties shown for *B* and *V* list the standard deviation of the mean of the measurements in that visit in parentheses for the final digits of the value. The formal uncertainty based on photon-counting noise is less than what is shown. Despite the apparently low uncertainties, the individual measurements in each visit show clear systematic trends relative to the mean of the visit. These trends are thought to be related to additional instrumental effects that are poorly understood, and no method for their removal has yet been found. As a result, these uncertainties do not reflect the underlying

Table 4
Visit-averaged *B* Photometry of Charon

JD Mid-time	*g* (deg)	Lat (deg)	Elon (deg)	*B* (mag)	Rotation Mag	Phase Mag
2452436.830645	0.361	29.38	180.55	18.0325(16)	17.8519	17.9747
2452787.598492	0.513	31.63	208.61	18.0711(07)	17.8526	18.0199
2452550.675166	1.712	28.33	244.21	18.1555(06)	17.8187	18.1383
2452799.240041	0.316	31.35	272.59	17.9615(14)	17.7948	17.9732
2452472.962867	1.238	28.55	304.38	18.0750(06)	17.7661	18.1043
2452772.598087	0.912	31.96	333.92	18.0648(09)	17.7853	18.0959
2452440.035934	0.410	29.30	359.93	17.9627(08)	17.7684	17.9920
2452688.541026	1.734	32.17	31.52	18.1065(07)	17.7687	18.1363
2452458.069952	0.858	28.86	63.66	18.0445(09)	17.7712	18.0736
2452789.643255	0.464	31.58	93.38	18.0151(14)	17.8074	18.0317
2452444.244973	0.499	29.19	122.74	18.0213(07)	17.8057	18.0109
2452750.247484	1.443	32.33	153.47	18.1703(09)	17.8477	18.1278

Table 5
Visit-averaged *V* Photometry of Charon

JD Mid-time	*g* (deg)	Lat (deg)	Elon (deg)	*V* (mag)	Rotation Mag	Phase Mag
2452436.862716	0.361	29.38	178.75	17.2993(26)	17.1485	17.2427
2452787.613817	0.513	31.63	207.75	17.3432(06)	17.1571	17.2901
2452550.702273	1.712	28.33	242.68	17.4266(08)	17.1217	17.4068
2452799.274918	0.316	31.35	270.63	17.2270(09)	17.0889	17.2397
2452472.996286	1.238	28.55	302.50	17.3429(07)	17.0672	17.3783
2452772.634032	0.911	31.96	331.89	17.3156(13)	17.0700	17.3533
2452440.068009	0.411	29.30	358.12	17.2341(07)	17.0705	17.2657
2452688.556350	1.734	32.17	30.66	17.3823(12)	17.0763	17.4076
2452458.097114	0.859	28.86	62.13	17.3168(10)	17.0772	17.3390
2452789.676579	0.463	31.58	91.51	17.2751(11)	17.0995	17.2881
2452444.277588	0.500	29.19	120.90	17.2916(07)	17.1081	17.2827
2452750.264898	1.442	32.33	152.49	17.4330(06)	17.1432	17.3933

photon-counting errors (which are much smaller) and cannot be considered definitive but we hope they are at least useful for relative weighting. The column labeled "rotation mag" is the rotational light curve after removing the effects of the changing Sun–Pluto–Earth (phase) angle. The column labeled "phase mag" is the phase variation in the photometry after removing the rotational light curve. These values will be discussed in detail later.

These light curves are superior to those from Buie et al. (1997) because the absolute calibration of the HRC images is good enough to stand on its own and does not need external calibration as was required by the earlier WFPC data. In particular, the quality of the Charon light curve is vastly better because the intrinsic signal-to-noise ratio is much higher, the PSF overlap between Pluto and Charon is almost nonexistent, and the photometric quality of HRC data is much better.

4.1. Light-curve Decomposition

The observed photometry is a complicated mixture of variations caused by surface albedo features, changes in sub-Earth and sub-solar latitude, and variations due to the changing solar phase angle. Small variations caused by the changing latitude are ignored in this analysis. The approach of Buie et al. (1997) was to fit a Fourier series expansion plus solar phase coefficient to the light-curve data. One of the surprises in the new ACS data was that a linear phase coefficient was not good enough to model the phase variations. The nonlinearity required a more advanced treatment. A standard H and G fit to the data might be sufficient, but given our work on modeling the surfaces of Pluto and Charon we needed to compute a phase curve based on a Hapke photometric model (Hapke 1993).

To fit the phase curve, we used a uniform sphere with a mean single-scattering albedo along with the surface compaction parameter h, the value of the single-particle phase function averaged over our phase angle range $\overline{P(g)}$, the backscatter coefficient B_0, and the average surface slope $\overline{\theta}$. Together these values describe a global response to changing solar phase angle. Note that for these calculations we do not include the effects of coherent backscatter and look for a good fit based only on the shadow-hiding components of the Hapke theory (Hapke 1993). While fitting the phase behavior, the mean single-scattering albedo is varied to get the absolute flux correct, but the phase behavior is largely determined by the other parameters. Note that the inclusion of $\overline{\theta}$ has a very small impact on the phase behavior but it is very important for the numerical integrations required in Paper II. It is used here for consistency with the calculations and results of the companion paper. The phase behavior could also be computed using coherent backscatter but as Schaefer et al. (2009) pointed out, the shape of the curve is nearly the same for shadow hiding and coherent backscatter. The purpose here is to use the Hapke theory as a functional form to fit the behavior.

Fitting the rotational modulations is done as before by a n-term Fourier series fit to the photometry (see Equation (2) in Buie et al. 1997). However, the nonlinear phase behavior was not simultaneously fit along with the Fourier series. To fit the data, we first fitted for a linear phase coefficient and the Fourier series. From this fit we separated the photometry into two components: rotational light curve at 0° phase and the phase curve at the light-curve mean. Next, the phase curve was fitted by the Hapke photometric model described above. This model was then subtracted from the original photometry leading to a new approximation of the rotational light curve after adding back the 0° phase magnitude. This new rotational light curve is refitted with a Fourier series, and the new series expansion is subtracted from the original photometry to retrieve a better phase curve. This process of alternately fitting phase and rotation was repeated until a final converged result emerged after just a few iterations. As a consequence of the longitude sampling pattern with respect to phase angle, there was no correlation between the rotational and phase light curves.

4.2. Color

Deriving the $(B - V)$ color for each object required special processing since the individual filter measurements were neither simultaneous nor interleaved. The process starts with the original measurements as corrected for distance but not for rotation or phase angle. Each *B* measurement is paired with a *V* measurement in the sequential order within a visit. For example, the first *B* measurement is paired with the first *V* measurement; the second *B* measurement is paired with the second *V* measurement; and so on. Each measurement is then corrected to 1° phase angle. Then, each *V* measurement is corrected for the slight difference in the sub-Earth longitude of the *B* measurement using the fitted Fourier series to compute the change between the time of the two points. The change in solar phase angle is negligible and is ignored at this step. Once corrected, each pair results in a single $(B - V)$ measurement that is tied to the time and geometry of the *B* measurement. These corrections are generally small and never exceed a 1% differential correction in the final answer but doing so improved the final results. The final visit-averaged

Table 6
Visit-averaged $B - V$ Color of Pluto and Charon

JD	Phase	Lat	Pluto		Charon	
Mid-time	Angle	(deg)	Elon (deg)	$B-V$ (mag)	Elon (deg)	$B-V$ (mag)
2452436.830645	0.361	29.38	0.55	0.957(17)	180.55	0.737(15)
2452787.598492	0.513	31.63	28.61	0.954(02)	208.61	0.730(03)
2452550.675166	1.712	28.33	64.21	0.956(04)	244.21	0.733(04)
2452799.240041	0.316	31.35	92.59	0.983(08)	272.59	0.742(07)
2452472.962867	1.238	28.55	124.38	0.969(04)	304.38	0.734(03)
2452772.598087	0.912	31.96	153.91	0.994(08)	333.92	0.749(08)
2452440.035934	0.410	29.30	179.93	0.949(03)	359.93	0.731(03)
2452688.541026	1.734	32.17	211.52	0.935(07)	31.52	0.726(06)
2452458.069952	0.858	28.86	243.66	0.939(03)	63.66	0.727(05)
2452789.643255	0.464	31.58	273.38	0.959(08)	93.38	0.741(09)
2452444.244973	0.499	29.19	302.74	0.947(05)	122.74	0.729(03)
2452750.247484	1.443	32.33	333.47	0.964(02)	153.47	0.738(03)

Table 7
B Light-curve Coefficients for Pluto

n	a_n	σ_a	b_n	σ_b
0	16.2832	0.0008	...	...
1	+0.0370	0.0010	+0.1102	0.0011
2	−0.0380	0.0013	−0.0379	0.0010
3	+0.0070	0.0011	+0.0098	0.0013
4	+0.0061	0.0017	−0.0020	0.0010
$\chi^2 = 194$				
$\overline{\lvert O-C\rvert} = 0.011$ mag				

color measurements are shown in Table 6. The geometry information from this table is identical to that shown in Tables 2 and 4. The values in parentheses are the uncertainties in the colors that match the last digits of the tabulated photometry. The choice of 1° phase angle for the color is not entirely arbitrary. The phase behavior of an object can be a function of the phase angle. Rather than citing a color as a function of phase angle, we chose a convenient phase angle that is interior to the current and historical photometric record for ease of comparison between our results and prior work.

5. PLUTO RESULTS

5.1. Pluto Light Curves

The new rotational light curves of Pluto ("rotation mag" from Tables 2 and 3) are plotted in Figures 1 and 2 while the coefficients from the Fourier series fits are shown in Tables 7 and 8. A comparison of the new Pluto light curves with the previous result from Buie et al. (1997) reveals some interesting changes. At both wavelengths, the light-curve amplitude has diminished as expected from the more pole-on aspect in the newer data. The dominant term in the Fourier series expansion is b_1 and has dropped from 0.1284 ± 0.0005 down to 0.1095 ± 0.0036 (B) and 0.0978 ± 0.0027 (V). The constant term (or mean, a_0) shows a rather striking trend. The B light curve shows a 4.5% decrease in overall brightness while the V light curve shows a 4% increase in brightness. This is seen in the plots where the new B light curve lies well below the previous light curve, and the new V light curve is at or above the old data. The amount of change is clearly a function of both longitude and wavelength. We will return to these results during the discussion of the color data.

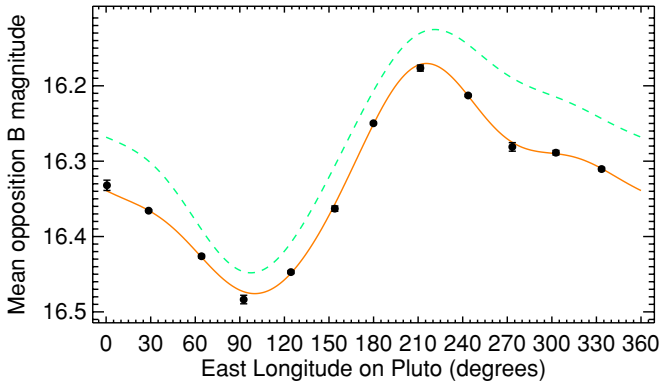

Figure 1. B Light curve of Pluto. All values in this figure are shown at 1° phase angle for mean opposition distance. The data points with errors are the visit-averaged measurements. The solid (orange) curve is the Fourier series representation using the fit in Table 7. The dashed (green) curve is the light curve from Buie et al. (1997). Subtract 0.0434 mag to correct the new data to 0° phase angle.

(A color version of this figure is available in the online journal.)

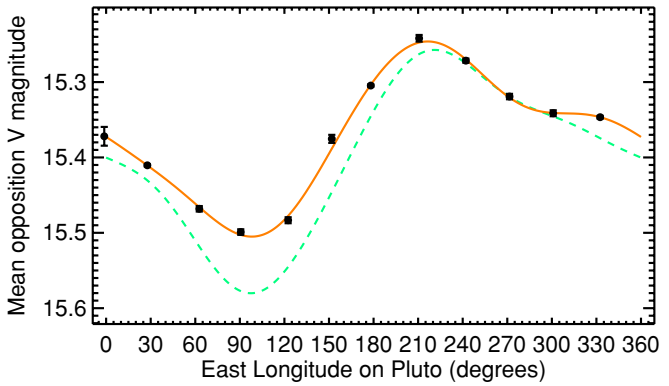

Figure 2. V Light curve of Pluto. All values on this figure are shown at 1° phase angle for mean opposition distance. The data points with errors are the visit-averaged measurements. The solid (orange) curve is the Fourier series representation using the fit in Table 8. The dashed (green) curve is the light curve from Buie et al. (1997). Subtract 0.0398 mag to correct the new data to 0° phase angle.

(A color version of this figure is available in the online journal.)

Table 8
V Light-curve Coefficients for Pluto

n	a_n	σ_a	b_n	σ_b
0	15.3298	0.0008	...	...
1	+0.0338	0.0011	+0.0969	0.0013
2	−0.0373	0.0012	−0.0247	0.0013
3	+0.0038	0.0015	+0.0046	0.0013
4	+0.0035	0.0016	+0.0033	0.0013
$\chi^2 = 212$				
$\overline{\lvert O-C\rvert} = 0.013$ mag				

5.2. Pluto Phase Behavior

When the Pluto phase behavior was fitted with a linear phase coefficient, we obtained $\beta_B = 0.0392 \pm 0.0064$ mag deg^{-1} and $\beta_V = 0.0355 \pm 0.0045$ mag deg^{-1}. Given the uncertainties, these measurements are consistent with the same phase coefficient for each filter. Combining these two measurements with a weighted mean, we determined $\beta = 0.0367 \pm 0.0037$ mag deg^{-1}. The previous value from Buie et al. (1997) was $\beta_V = 0.0294 \pm 0.0011$ mag deg^{-1}. These measurements indicate a 2σ change in β of +0.007 mag deg^{-1} between 1993 and 2003.

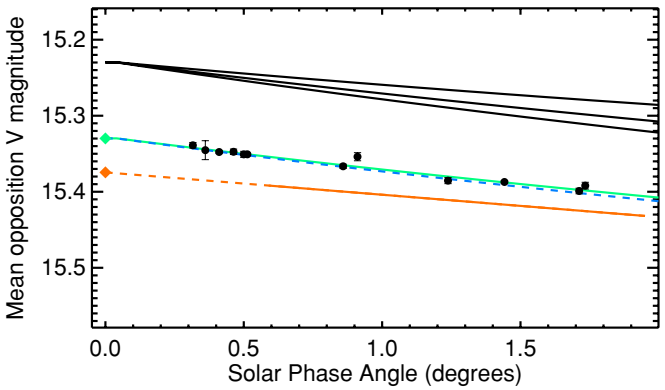

Figure 3. Phase curve for Pluto. The solid points with errors show the *V* photometry after the rotational light curve has been removed. The solid (green) curve that touches these points is a nonlinear Hapke fit to the *V* data. The dashed (blue) curve is the fit to the *B* data after shifting to match the zero-phase magnitude of the *V* fit. The bottom (orange) curve is the linear fit from Buie et al. (1997) and is solid over the phase angle covered by those data, and the dashed portion is the extrapolation to zero phase. The diamonds indicate the fitted zero-phase magnitude for the respective fits. The three solid (black) curves at the top show the phase behavior of a uniform sphere with single-scattering albedos of 0, 0.7303, and 1.0 keeping all other scattering parameters the same as the fitted values for the *V* data. These three curves have been vertically offset for clarity as well as shifted so that the zero-phase magnitudes are the same.

(A color version of this figure is available in the online journal.)

Table 9
Global Hapke Parameters

Body	Filter	h	$\overline{P(g)}$	B_0	$\overline{\theta}$	χ^2	$\langle w \rangle$
Pluto	*B*	0.0790[2]	2.96[1]	0.790[5]	10[x]	194	0.5973
($R = 1153$ km)	*V*	0.0790[2]	2.83[1]	0.790[5]	10[x]	212	0.7303
Charon	*B*	0.0033[2]	3.02[1]	0.585[5]	20[x]	235	0.5942
($R = 606$ km)	*V*	0.0044[2]	2.46[1]	0.600[5]	20[x]	191	0.6737

As we shall see more convincingly with the Charon data, this apparent change in β does not necessarily mean that the surface properties have changed. The change can be readily explained by the differing range of solar phase angles combined with a nonlinear phase curve. The photometric behavior with solar phase angle ("phase mag" from Tables 2 and 3) is shown in Figure 3. The first thing to note in these new data is that the range of solar phase angle is larger than it was for Buie et al. (1997). The previous data ranged from 0.°59 to 1.°95. The new data range from 0.°32 to 1.°74 and half of the new data are at smaller phase than was possible in 1993.

The trends shown in Figure 3 show just how small the difference is between the 1993 and the 2003 results. While the new value for β is clearly a better fit, the misfit to the old value is subtle. The solid (green) curve in this figure shows the phase behavior of a uniform sphere with the set of Hapke parameters as tabulated in Table 9. Only the *V* data are plotted since the phase behavior is essentially the same for both filters. The dashed blue curve is a linear fit to the points. The Hapke-based curve is clearly nonlinear but only slightly so. The bottom orange curve shows the linear fit to the 1993 data. In this curve, the range of constraint is indicated with a solid curve, and its extrapolation to zero phase is dashed. If the linear fit to the new data is constrained to the same range of phase angles, the resulting slope is the same as the older data. Though the difference is small, the goodness of fit is better for the nonlinear Hapke-based fit. The relevant point of this figure is that the apparent upward trend to β is most likely a direct consequence of a linear fit to a larger range of nonlinear data rather than any intrinsic change in surface properties.

Table 10
$B - V$ Color Fitting

Value	Pluto	Charon
Mean ($B - V$)	0.9584(23)	0.7327(19)
Weighted mean	0.9540(10)	0.7315(13)
$N = 2$, χ_r^2	1.4	1.1
a_0	+0.9564(11)	+0.7328(13)
a_1	+0.0024(13)	−0.0002(19)
b_1	+0.0117(17)	−0.0026(19)
a_2	−0.0020(15)	+0.0001(20)
b_2	−0.0117(14)	−0.0036(17)
$\overline{\lvert O - C \rvert}$	0.021	0.020

The three solid (black) curves at the top of the figure show the phase curves implied by the Hapke parameters for three different global single-scattering albedos ($w = 0.0$, 0.7303, 1.0) but adjusting all to the same fictitious zero-phase magnitude to offset them from the data. As these curves show, the phase behavior variation with w is larger than the difference between linear and nonlinear descriptions. This information clearly indicates that the assumption of global Hapke scattering parameters is weak given the large range of w in all surface maps of Pluto. However, the data possible from our Earth-based vantage are insufficient to uniquely model this more complicated photometric behavior, and we are stuck with a simpler, less-accurate methodology.

5.3. Pluto Color

We analyzed the visit-averaged ($B - V$) color of Pluto versus longitude from Table 6. These results are summarized in Table 10. The uncertainties in all quantities are shown in parentheses for the trailing digits of the value. The unweighted mean of all data was used for all photometric transformations. The weighted mean is also shown for Pluto but this value is of little use since there is clearly significant variation of color with longitude. A two-term Fourier fit (with no phase component) is shown. Other fits with differing numbers of terms had larger values of χ_ν^2.

The color light curve of Pluto is shown in Figure 4. The three-dot-dash (orange) curve is the two-term Fourier fit, while the solid (blue) curve is the color light curve from differencing the two individual *B* and *V* four-term fits. This figure clearly shows that the color for Pluto is now redder at all longitudes compared to that seen in Buie et al. (1997) and that the color is now seen to vary significantly with longitude. The mean value from 1992/1993 was ($B - V$) = 0.8675 ± 0.0014 and now the value from 2002/2003 is 0.9584 ± 0.0052. Further discussion on this result follows the introduction of the Charon results.

5.4. Pluto Time Variability

The light curves from Figures 1 and 2 can be compared in a different manner against the light curve of Buie et al. (1997). The Fourier fits to the light curves provide a measurement proportional to albedo as a function of longitude. Figure 5 shows the change in the *B* and *V* light curves using the older data as a reference. If there were no change, the albedo ratio would plot as unity. Values greater than 1 indicate an increase in the hemispherically averaged albedo while values below 1 indicate a decrease. Except for the region near 270° the *V* data show a systematic increase in albedo with a peak change of just over 7%. The *B* data clearly show a decrease in albedo where the least

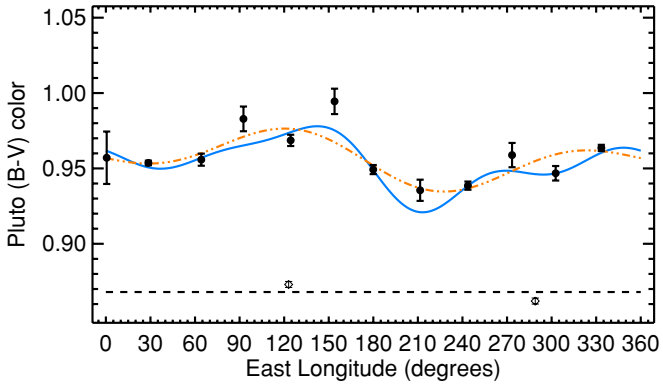

Figure 4. ($B - V$) color light curve of Pluto. The solid points are the per-visit color measurements computed after correcting the B values to 1° phase and correcting the V values to 1° phase and to the same longitude as the B measurements using the fitted V light curve. The solid (blue) line shows the color from the difference of the B and V Fourier series fits. The three-dot-dash (orange) line is a two-term Fourier fit to the solid points. The dashed line shows the mean color of Pluto from Buie et al. (1997) shown with the individual measurements (diamonds) that defined the mean.

(A color version of this figure is available in the online journal.)

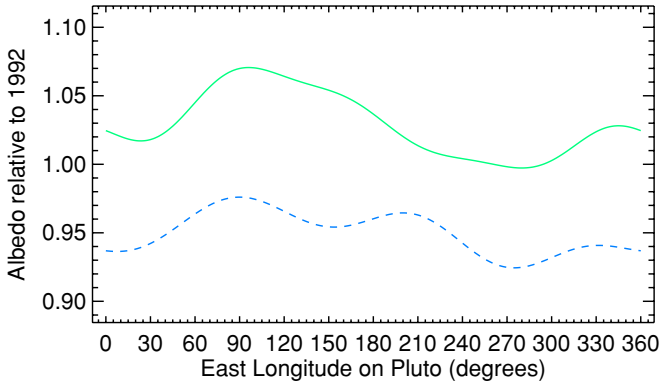

Figure 5. Albedo change on Pluto. The solid (green) curve shows the change in V albedo of Pluto at 1° phase between the 1992and 1993 light curve of Buie et al. (1997) and the 2002–2003 light curve from this work. The dashed (blue) curve shows the change in the B albedo for the same data sets assuming a constant color for the 1992–1993 data.

(A color version of this figure is available in the online journal.)

change is just 2% at 80° (near minimum light) and the largest change is nearly 8% near 270° longitude.

The marked change we observed in color from 2000 to 2003 makes it seem likely that the color and light curve could have been changing during the 12 months of observation as well. As a test, we computed light-curve residuals by subtracting the rotational light curve and the phase curve from the original photometry. Figure 6 shows these residuals as a function of time where the trend is an increase in the B magnitude with time while the V magnitude is seen to decrease. Figure 7 show trends as a function of sub-Earth latitude and here the B magnitude is seen to increase with increasing latitude and the V decreases. None of these trends are strong but these plots serve to provide guidance to future observational efforts.

While the individual filter measurements are inconclusive, the overall color shows a more significant result. Splitting the data into two groups by their time order gives us a global color at two distinct epochs. The early set is at a mean sub-Earth latitude of 28°.89 and gives a weighted mean $(B - V) = 0.9503 \pm 0.0016$. The later set is at a mean sub-Earth latitude of 31°.96 and has a weighted mean of $(B - V) = 0.9598 \pm 0.0013$. The color change from these averages is thus $(B-V)_{2003} - (B-V)_{2002} =$

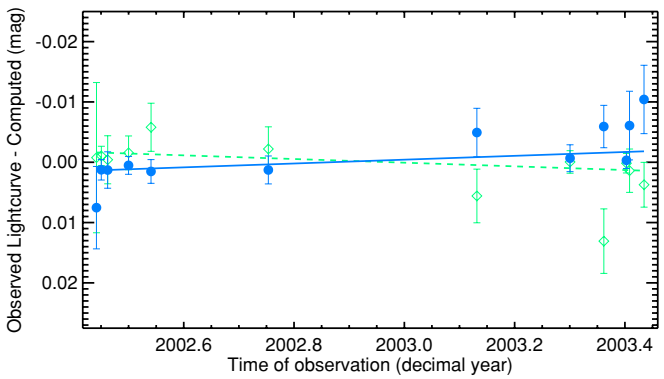

Figure 6. Pluto light-curve residuals after removing rotational light curve and solar phase curve as a function of time. The solid dots (blue) show the B residuals and the diamonds (green) show the V residuals. The fitted slope (solid, blue curve) for B is -0.0032 ± 0.0016 mag yr^{-1}. The fitted slope (dashed, green curve) for V is 0.0030 ± 0.0018 mag yr^{-1}. These trends, if real, indicate a brightening in B with time with a suggestion of accelerated change at the end of the observations. The V residuals show a weak downward trend.

(A color version of this figure is available in the online journal.)

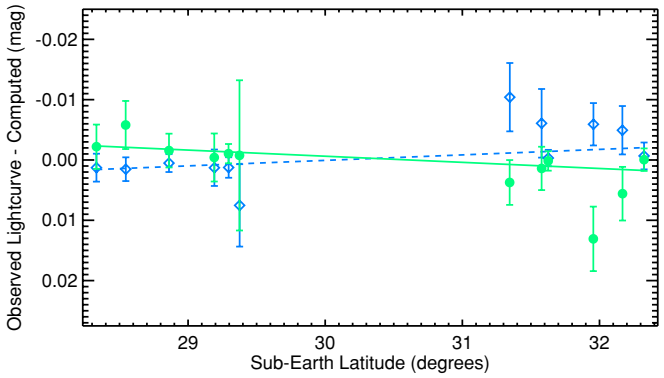

Figure 7. Pluto light-curve residuals after removing rotational light curve and solar phase curve as a function of sub-Earth latitude. The solid dots (green) show the V residuals and the diamonds (blue) show the B residuals. The fitted slope (solid, green curve) for V is 0.0010 ± 0.0005 mag deg^{-1}. The fitted slope (dashed, blue curve) for B is -0.0009 ± 0.0004 mag deg^{-1}. These trends, if real, indicate a gradual brightening in V with increasing sub-Earth latitude while B shows the opposite trend.

(A color version of this figure is available in the online journal.)

0.0095 ± 0.0021. Converting to a rate of change implies a rate of 0.0031 ± 0.0007 mag per degree of latitude (redder as sub-Earth latitude moves away from the equator) or a rate of 0.0115 ± 0.0025 mag per year (redder with increasing time). If we assume the color change started just after the 2000 ground-based observations, the new mean color implies a total change of 0.0865 ± 0.0017 mag and a rate of change of $\sim$0.016 mag deg^{-1} or $\sim$0.029 mag yr^{-1}. These two sets of rates are clearly not the same indicating the change is likely to be complex and poorly mapped out by these observations alone.

6. CHARON RESULTS

6.1. Charon Light Curves

The new V light curve of Charon is shown in Figure 8, and the Fourier series fits are shown in Tables 11 and 12. The construction of this figure is the same as for Pluto. The agreement between these new results and the Buie et al. (1997) result is excellent. The new observations are clearly of much higher quality, and the basic structure of the light curve seen previously is confirmed. The amplitude of 8% is confirmed

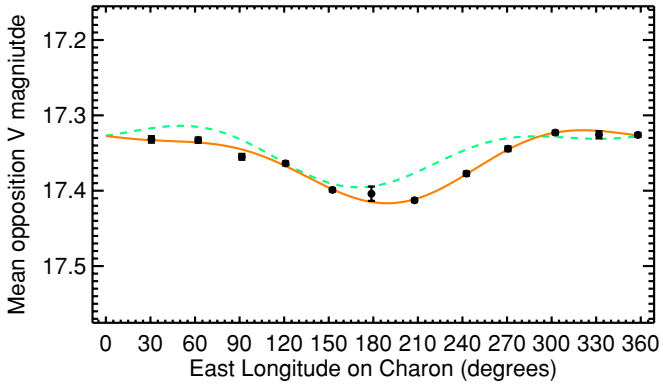

Figure 8. *V* Light curve of Charon. All values on this figure are shown at 1° phase angle for mean opposition distance. The data points with errors are the visit-averaged measurements. The solid curve is the Fourier series representation using the fit in Table 12. The dashed curve is the light curve from Buie et al. (1997). Subtract 0.2549 mag to correct the new data to 0° phase angle.

(A color version of this figure is available in the online journal.)

Table 11
B Light-curve Coefficients for Charon

n	a_n	σ_a	b_n	σ_b
0	17.7935	0.0009	...	...
1	−0.0435	0.0013	−0.0048	0.0013
2	+0.0142	0.0014	+0.0036	0.0012
		$\chi^2 = 235$		
		$\overline{\lvert O-C\rvert} = 0.013$ mag		

Table 12
V Light-curve Coefficients for Charon

n	a_n	σ_a	b_n	σ_b
0	17.0978	0.0009	...	...
1	−0.0440	0.0013	−0.0009	0.0013
2	+0.0129	0.0013	+0.0078	0.0013
		$\chi^2 = 191$		
		$\overline{\lvert O-C\rvert} = 0.013$ mag		

and the mean value is consistent between the two observations. These results also confirm that the surface of Charon is slightly darker on the anti-Pluto hemisphere or, conversely, brighter on the Pluto-facing hemisphere. As with the earlier results, the light curve is best represented by a two-term Fourier fit.

6.2. Charon Phase Behavior

The size of the phase correction for Charon is much more pronounced than was seen for Pluto. In fact, the photometric variation seen on Charon over one apparition is dominated by the phase behavior, and a well-sampled data set is required to accurately decompose the two effects. Our new phase curve for Charon is shown in Figure 9. The data (solid black points with error bars) clearly show a nonlinear trend as a consequence of including data at lower phase angles than previously seen. The solid green curve is the Hapke-based *V* model fit whose parameters are tabulated in Table 9. The dashed blue curve is the *B* model fit adjusted to the same zero-phase magnitude. The linear (orange) curve is the fit from the 1993 data without any photometric adjustment. Again, the solid portion of the curve is the region of constraint in the older data while the dashed portion is the linear extrapolation to zero phase. The linear fit is quite similar to the nonlinear fit over the more restricted phase angle range. Clearly, the phase behavior cannot be adequately described by a linear trend as is still possible for Pluto.

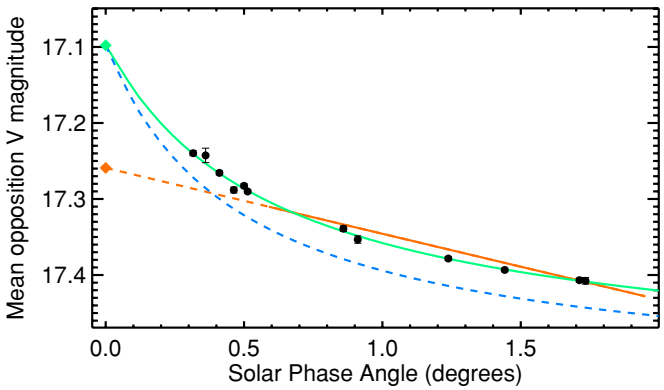

Figure 9. Phase curve for Charon. The solid points with errors show the *V* photometry after the rotational light curve has been removed. The solid (green) curve that touches these points is a nonlinear Hapke fit to the *V* data. The dashed (blue) curve is the fit to the *B* data after shifting to match the zero-phase magnitude of the *V* fit. The straight (orange) line is the linear fit from Buie et al. (1997) and is solid over the phase angle covered by those data, and the dashed portion is the extrapolation to zero phase. The diamonds indicate the fitted zero-phase magnitude for the respective fits.

(A color version of this figure is available in the online journal.)

6.3. Charon Color

Table 10 shows the fitting results for the Charon color data. The weighted mean for Charon is our final adopted value where we find $(B - V) = 0.7313 \pm 0.0017$. The Charon $(B - V)$ data from Table 6 are plotted in Figure 10. The formal Fourier fit color light curve with $N = 2$ is shown (three-dot-dash orange curve). The difference of the *B* and *V* fitted light curves is shown with the solid (blue) line. The vertical shift between the two curves is a consequence of the mean phase angle represented by the two methods. If these two are corrected to the same phase angle, they become virtually indistinguishable. The color variation with longitude implied by these fits is very small (<1%). This new color determination is formally slightly redder than that found in Buie et al. (1997)—the old value was 0.710 ± 0.011 (shown with the dashed black line) and differs by 1.9σ. This difference cannot be explained by the differing mean phase angle of the two data sets. There has been a significant shift in the sub-Earth latitude, and this could be an indication of a color difference between the two poles of Charon. However, the older data set required a model to establish the absolute calibration and the color is slightly suspect. We believe it is more likely that this newer value simply reflects a better measurement and the apparent color change is not likely to be real.

7. FINAL COMMENTS ON COLOR

The change in Pluto color is much larger than the 2% systematic error in color noted for Charon. This large change in color was a source of great concern to us, particularly since a change this large could have been easily seen and would have been reported by complementary ground-based observing projects (Buie & Grundy 2000; Buratti et al. 2003). Instead, these prior efforts showed a $(B-V)$ color in 2000 that is identical to what has been seen since Pluto's discovery. While it is true that the absolute photometry from these new data depends critically on the photometric transformations for ACS/HRC, we can find no plausible explanation for the close agreement between the multi-epoch Charon results and change in the Pluto color, especially given that both objects are simultaneously observed. If all the results are correct, the most likely explanation for

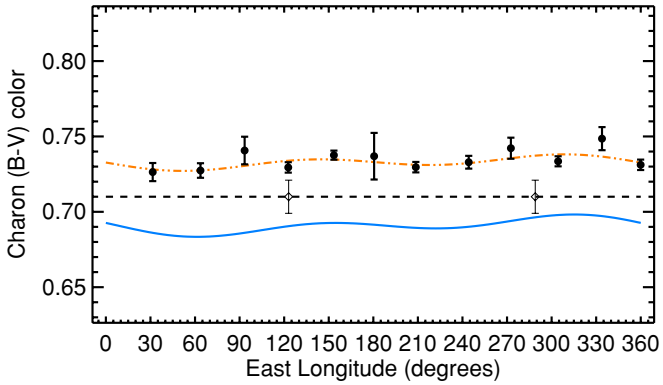

Figure 10. ($B - V$) color light curve of Charon. The solid points are the per-visit color measurements computed after correcting the B values to 1° phase and correcting the V values to 1° phase and to the same longitude as the B measurements using the fitted V light curve. The solid (blue) line shows the color from the difference of the B and V Fourier series fits (this is the 0° phase color). The three-dot-dash (orange) line is a two-term Fourier fit to the solid points and ranges between 0.726 and 0.749. The dashed curve shows the mean color of Charon from Buie et al. (1997) shown with the individual measurements (diamonds) that defined the mean.

(A color version of this figure is available in the online journal.)

these data remains that there is widespread color change taking place on the surface of Pluto and furthermore this change took place between 2000 and 2003. Finally, we note that the Buie et al. (1997) result provided a ($B - V$) measurement at two longitudes that indicated a slightly redder color near minimum light. These newer color measurements clearly show a variation of ±2% with longitude where the reddest color is centered on minimum light and the least red color is centered on maximum light.

8. CONCLUSIONS

That we are seeing change in the light curve of Pluto should come as no surprise. Clearly, the photometric record following the first light curve reported in 1955 shows that the light curve of Pluto changes dramatically with orbital longitude. The decade surrounding the mutual event season made it appear as though Pluto was really an unchanging object. When considering the data from 1954 to 1990, it was still possible to explain all of these changes using only geometry. These new observations now clearly show that time variability must be included for a more accurate description of the surface of Pluto.

Geometry must still play a role in the observed data set. There is no escaping the fact that the viewing and illumination geometry vary and in turn cause strong changes. Untangling the geometric and temporal components of the photometric record is still a daunting task but with continued monitoring, the upcoming 2015 encounter of New Horizons with Pluto, and further modeling we may yet be able to more fully describe the progression of seasonal surface and atmospheric processes through a full Plutonian year.

The implicit assumption for understanding the temporal evolution of the photometry is that this is somehow related to, if not driven by, surface and atmosphere interactions though volatile migration. The albedo patterns, color changes, and atmospheric structure variations as driven by seasonal forcing from solar illumination are all intimately connected, and one can hope that a comprehensive model will one day incorporate and explain the ever growing observational record.

We now have two confirmed epochs of variation with interesting differences in the conditions present at the time of change. The first epoch is between 1933 and 1954 when Pluto was at an epoch of nearly constant high sub-solar latitude and systematically decreasing heliocentric distance. Over this period, we saw a surface decreasing in mean albedo without any apparent change in color. That this color remained unchanged until 2000 is also an important clue into the surface evolution (or lack there of).

The second epoch (present day) is just after perihelion when the heliocentric distance is at a minimum giving rise to peak insolation. At this time, the distance is essentially constant but the illumination geometry is changing at its fastest rate. The pole that had been in a long period of winter darkness is now moving to unending illumination while the other pole becomes a systematic sink for volatiles as it begins its own period of winter. In 1986, Pluto passed its equinox and for the next 14 years optical photometry did not appear to be changing except for a slight and subtle light-curve evolution. All of a sudden, the surface color changed between 2000 and 2002 while the light curve is also showing significant changes. The new data also clearly show these changes must be global. The timing, rate of change, and magnitude of these variations will all be important constraints on future models that would hope to describe the volatile transport and its effect on the surface. The sudden onset of the change in color suggests that perhaps we have just seen some overcoating on the sunlit pole sublimating off, revealing a previously obscured layer. Such changes are clearly consistent with global transport of material but continued observations are critical to help constrain and understand this complicated system.

An additional and equally important constraint on these speculations is the spectroscopic record since it directly constrains the volatile inventory in the topmost layers of the surface. These new photometric results indicate that a new reddening agent is coming into view (either by geometry, removal of an overcoat, or in situ formation). How the spectroscopic record changes will be an important factor in understanding Pluto's surface. An explanation is beyond the scope of this work but clearly argues for continued photometric and spectroscopic monitoring.

Our new observations provide an essential confirmation of the light curve of Charon and also clearly show a longitudinally uniform coloring of its surface. The color we now see is very slightly redder than what was seen in 1992. However, as we mentioned earlier, this small change may be due to unavoidable errors in photometric transformation, or this change could be real. If so, this would indicate that the pole coming more into view is redder than the global color. Furthermore, this would require that the pole leaving our view is less red than the pole coming into view, otherwise the two terrains would cancel each other, and the hemispherical color would not change with aspect. Additional observations will clearly help but the best source of future information will clearly be the New Horizons mission.

Our confirmation of Charon's light curve leaves us with an intriguing observable that the light curve is symmetric with respect to the sub-Pluto hemisphere. A more common albedo pattern on tidally locked satellites in the outer solar system is a leading/trailing asymmetry that arises from orbital motion but perhaps the unusually slow orbital motion (∼200 m s^{-1}) is not fast enough to generate the "normal" pattern. Instead, this light-curve pattern argues for a process not influenced by orbital motion. It could be similar to the Earth's Moon where a mass

distribution is coupled to both the tidally locked orientation and a surface expression with an albedo signature. Perhaps, it arises from the thermal radiation from Pluto on the Pluto-facing hemisphere. Another scenario could be an implantation process driven by mass loss from the top of Pluto's atmosphere. But, the escaping flow and the resulting process must operate with a flow pattern that is fast with respect to orbital motion.

These new observations continue to highlight the differences between the surfaces of Pluto and Charon. Since the mutual event season we have known of a water–ice-dominated surface for Charon while Pluto has a surface largely covered by mobile volatile species. We knew from the 1992 *HST* observations (Stern et al. 1997) that they had markedly different phase coefficients. But, the new phase data bring that contrast into even sharper focus. The Pluto phase curve continues to show a shallow rise with decreasing phase angle and a very slight nonlinearity. This behavior combined with the lack of color variation with changing phase angle argues that the opposition effect on Pluto over the current phase angle range is dominated by shadow hiding. There is still room within unsampled phase angle ranges for a substantial opposition surge that, if seen, would be consistent with coherent backscatter (Schaefer et al. 2009). Continued observations are clearly warranted but will be difficult without separate observations as are afforded by *HST*. In contrast, the phase behavior of Charon is now seen to be strongly nonlinear and is also clearly dependent on wavelength. Both of these results indicate that the observed surge is most likely due to coherent backscatter (Schaefer et al. 2009) even though we have modeled the variation exclusively with the shadow-hiding portion of the Hapke theory.

The Hapke parameters for each body are also seen to be distinct and the most significant difference is the large value for h on Charon. The other Hapke parameters are clearly different but inverting this knowledge into a direct understanding of the surface properties is hampered by not fully accounting for coherent backscatter. The difference between Pluto and Charon is consistent with the general phase behavior seen for most objects—lower albedo surfaces have a large phase variation (e.g., Schaefer et al. 2009). Once again, we look forward to new information from New Horizons to give us the means to develop more precise models that can more fully constrain surface properties and processes.

This paper is based on observations with the NASA/ESA *Hubble Space Telescope* obtained at the Space Telescope Science Institute, which is operated by the Association of Universities for Research in Astronomy, Incorporated, under NASA contract NAS5-26555. Support for this work was provided by NASA through grant numbers HST-GO-09391.01-A, HST-GO-10786.01, and HST-AR-10940.01 from STScI. Special thanks to the late Andy Lubenow (1956–2005) at STScI for his exemplary support of this project.

REFERENCES

Binzel, R. P., & Hubbard, W. B. 1997, in Pluto and Charon, ed. D. J. Tholen & S. A. Stern (Tucson, AZ: Univ. Arizona Press)
Buie, M. W., & Bus, S. J. 1992, Icarus, 100, 288
Buie, M. W., & Grundy, W. M. 2000, BAAS, 32, 1083
Buie, M. W., Grundy, W. M., Young, E. F., Young, L. A., & Stern, S. A. 2006, AJ, 132, 290
Buie, M. W., Tholen, D. J., & Wasserman, L. H. 1997, Icarus, 125, 233
Buie, M. W., Young, E. F., & Binzel, R. P. 1997b, in Pluto and Charon, ed. D. J. Tholen & S. A. Stern (Tucson, AZ: Univ. Arizona Press)
Buratti, B. J., et al. 2003, Icarus, 162, 171
Grundy, W. M., & Buie, M. W. 2001, Icarus, 153, 248
Grundy, W. M., & Stansberry, J. A. 2000, Icarus, 148, 340
Hansen, C. J., & Paige, D. A. 1996, Icarus, 120, 247
Hapke, B. 1993, Combined Theory of Reflectance and Emittance Spectroscopy (Cambridge: Cambridge Univ. Press)
Krist, J. 2004, http://www.stsci.edu/software/tinytim/tinytim.html
Marcialis, R. L. 1997, in Pluto and Charon, ed. D. J. Tholen & S. A. Stern (Tucson, AZ: Univ. Arizona Press)
Schaefer, B. E., Buie, M. W., & Smith, L. T. 2008, Icarus, 197, 590
Schaefer, B. E., Rabinowitz, D. L., & Tourtellotte, S. W. 2009, AJ, 137, 129
Sirianni, M., et al. 2005, PASP, 117, 1049
Stern, S. A., Buie, M. W., & Trafton, L. M. 1997, AJ, 113, 827
Stern, S. A., Trafton, L. M., & Gladstone, G. R. 1988, Icarus, 75, 485
Tholen, D. J., Buie, M. W., Grundy, W. M., & Elliot, G. T. 2008, AJ, 135, 777
Trafton, L. M., Matson, D. L., & Stansberry, J. A. 1998, ASSL, Vol. 227, Solar System Ices (Dordrecht: Kluwer), 773
Walker, M. F., & Hardie, R. H. 1955, PASP, 67, 224
Young, E. F., et al. 2008, AJ, 136, 1757